J Mater Sci (2010) 45:546–551
DOI 10.1007/s10853-009-3972-z

Influence of annealing on the electrochemical behavior of finemet amorphous and nanocrystalline alloy

Hossein Asghari Shivaee · Ahmad Nozad Golikand · Hamid Reza Madaah Hosseini · Mehdi Asgari

Received: 9 August 2009 / Accepted: 8 October 2009 / Published online: 3 November 2009

Abstract The electrochemical corrosion behavior of finemet alloy at various heat treatment temperatures was investigated. Thermal behavior and structural changes were studied using differential scanning calorimetry and X-ray diffractometry, respectively. The electrochemical corrosion of amorphous and annealed samples was investigated in 0.10 M NaOH solution using electrochemical impedance spectroscopy and linear sweep voltammetery. Changes in morphology of the samples before and after corrosion were characterized using optical microscope. The results showed that structural relaxation and nanocrystallization during the heat treatment improved corrosion behavior of the alloy. The heat-treated alloy at 650 °C showed a corrosion rate of 1.37×10^{-8} A cm^{-2} and a positive shift of +417 mV in the corrosion potential compared to the amorphous alloy. Also, the heat-treated alloy at 650 °C showed a higher charge transfer resistance up to 50 kΩ due to corrosion resistance, compared with amorphous sample that showed a charge transfer resistance of 0.5 kΩ.

H. A. Shivaee
Institute for Nanoscience and Technology, Sharif University of Technology, Tehran, Iran

A. N. Golikand (✉) · M. Asgari
Electrochemistry and Fuel Cell Lab, NSTRI, Tehran, Iran
e-mail: anozad@aeoi.org.ir; ahmadnozadgolikand@yahoo.com

H. R. M. Hosseini
Department of Materials Science and Engineering, Sharif University of Technology, Tehran, Iran

Introduction

The finemet-type soft magnetic nanocrystalline alloys are among the softest magnetic materials known so far. These nanocrystalline alloys are produced by melt spinning (for making amorphous precursor) and subsequent heat treatment. Under the appropriate heat treatment conditions, magnetic FeSi nanograins will emerge from the amorphous matrix which results in ultrafine FeSi grains (10–20 nm) embedded in the matrix [1–3]. Both Cu and Nb play an important role in the formation of this structure. Cu promotes nucleation of FeSi nanograins and Nb acts as grain growth inhibitor. Also B and Si promote glass forming ability of the alloy. The excellent soft magnetic properties of the alloy are directly correlated to its ultrafine structure [4–10].

Because of excellent soft magnetic properties and wide range of applications such as transformers, sensors, and inductors, finemet-type alloys have been the object of much scientific and technological attention during the recent years [11, 12]. While the magnetic properties, nanocrystallization kinetics, and crystallization mechanism of these alloys have been studied extensively, no much work has been performed concerning the characterization of their electrochemical and corrosion properties [1, 8–10]. Since finemet is an iron-base alloy, investigation of electrochemical and corrosion behavior is necessary for developing its industrial application. Some studies have been published in this area, mainly relating to the effects of substitution of alloying elements on the electrochemical behavior of finemet-type alloys [13–20]. This study aims to describe the effects of heat treatment on the electrochemical behavior of finemet alloy using electrochemical impedance spectroscopy (EIS) in NaOH solution. The study of correlation between the structure and the corrosion behavior of the alloy is another important aim of this work.

Experimental

The ingot of master alloy was prepared by vacuum arc melting of the pure elements (99.99%) under argon atmosphere according to the $Fe_{73.5}Si_{13.5}B_9Cu_1Nb_3$ (at.%) nominal composition. Amorphous ribbons with a cross section of 0.02 × 1.00 mm were prepared by melt spinning under protective argon atmosphere. For this purpose, the alloy ingot was remelted in a quartz tube, and then was ejected from a nozzle onto a rotating copper wheel at the speed of 30 m s^{-1}. The actual composition of the amorphous ribbons was determined by inductively coupled plasma analysis. The amorphous nature of the ribbons was analyzed using X-ray diffraction (XRD; Philips model PW1800, Netherland) with CoK_α (1.78897 Å) radiation. In order to have estimation of the thermal behavior and phase transformations of the alloy, the crystallization behavior of amorphous alloy was investigated by a differential scanning calorimetry (DSC) instrument (Rheometic Scientific, model STA, UK) using continuous heating regime. Heat treatment of the samples was carried out at 250, 350, 450, 550, 650, and 750 °C. To prevent oxidation during the heat treatment, the samples were sealed in quartz ampoules after repeated evacuation sequences. The sample-containing ampoules were placed within the uniform heating zone of the furnace and annealed for 1 h. XRD patterns and resistivity measurements were used to study the structural changes during the heat treatment. Microstructure of the samples before and after treating with 0.10 M NaOH was investigated using optical microscope.

The electrochemical experiments were performed in a conventional three-electrode cell using an Autolab potentiostate/galvanostate model 30(2) controlled by GPES and FRA for potentiostatic and EIS, respectively. The samples of 4 mm^2 geometric areas were used as working electrodes. Electrode potentials were measured versus an Ag/AgCl reference electrode and a platinum wire was employed as a counter electrode. The impedance data of the finemet alloy after heat treatment in different temperatures were obtained after holding the samples in 0.10 M NaOH solutions at open-circuit potential for 1 h. The frequency ranged from 100 kHz to 0.01 Hz when the currents were steady, superimposing 10 mV AC amplitude over the stabilization potential of each sample. Zview software was used for analysis of the obtained results.

Results and discussion

Figure 1 shows the DSC curve of the alloy at a heating rate of 10 °C min^{-1}, where two exothermal peaks corresponding to different stages of crystallization can be seen. The first peak corresponds to the nanocrystallization of the

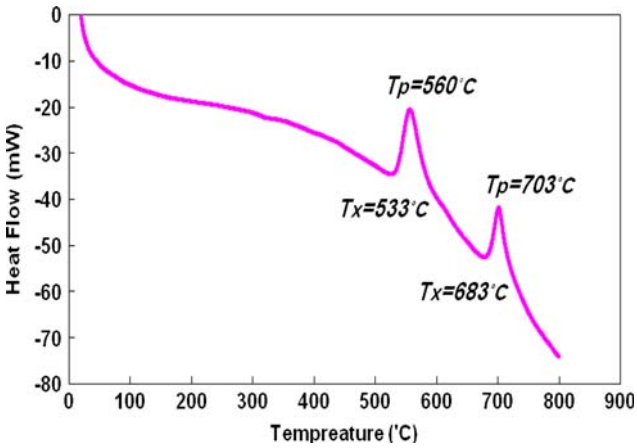

Fig. 1 DSC of the finemet alloy at 10 °C min^{-1}

FeSi soft magnetic phase and the second one relates to the appearance of boride-type phases (Fe_3B or Fe_2B) [4]. Formation of boride phases due to high value of magnetocrystalline anisotropy destruct soft magnetic properties and must be avoided by adjusting the annealing temperature. Thermal parameters such as onset crystallization temperature, T_x, and the peak temperature, T_p, are shown in Fig. 1.

Figure 2 shows XRD patterns of the amorphous and isothermally annealed samples. As shown in this figure, annealing of the alloy as quenched samples up to 450 °C caused no changes in the structure of the samples and only the amorphous halo peak could be seen. Then from 550 °C, FeSi nanocrystalline phase was formed within the amorphous matrix. In accordance with DSC measurements, the sample annealed at 650 °C merely contained FeSi nanocrystalline phase. Also, by increasing the annealing temperature to 750 °C, the new phases such as Fe_2B, $Fe_{23}B_6$, $Fe_{3.5}B$, and NbB_2 were precipitated.

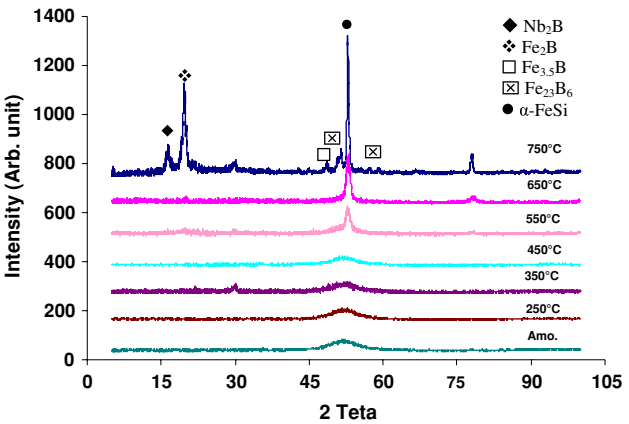

Fig. 2 XRD patterns of the amorphous samples and the samples annealed at various temperatures

The average crystallite size of the FeSi grains was calculated from the full-width at half-maximum of the (110) reflection using the Scherrer formula:

$$\langle D\rangle = \frac{K \cdot \lambda}{B \cdot \cos\theta} \quad (1)$$

where K is constant, λ is wavelength of the used X-ray, B is full-width at half-maximum of the selected peak, θ is Bragg angle, and $\langle D\rangle$ is mean diameter of the crystallites. Using this formula and considering instrumental line broadening and also absence of strain in the annealed samples, the average crystallite size of the samples annealed at 550 and 650 °C was obtained as 14 and 19 nm, respectively.

The results of electrical resistivity measurements were used to clarify the details of structural changes. As shown in Fig. 3, resistivity of the samples decreases with full nanocrystallization of the sample at 650 °C. This is mainly due to the ordered structure of nanograins in comparison with the disordered structure of amorphous state. In glassy metals, the mean-free path of conduction electrons is of the order of the interatomic distance and the electrical resistivity is consequently increased with respect to crystalline material [21]. Thus, the significant decrease in resistivity of the sample annealed at 350 °C could be due to the structural relaxation processes. As it is known, the structure relaxation precedes the crystallization, which is accompanied by the release of free volume and hence by the change in the mean interatomic distance [20, 23]. Also, resistivity of the sample heat treated greater than 350°C increased. This was not expected. It seems that Curie temperature behavior and high positive saturation magnetostriction coefficient of the amorphous phase ($\lambda_s \approx +23 \times 10^{-6}$) could be responsible for such behavior. Curie temperature of the amorphous phase is about 350 °C, which slightly increases due to structural relaxation [21, 22]. The samples annealed at the temperatures above Curie temperature bear a high level of stress during cooling when passing Curie temperature due to magnetostrictive force. This stress increases the resistivity of the sample. After nanocrystallization, negative magnetostriction coefficient of FeSi nanograins neutralized the high positive saturation magnetostriction coefficient of the amorphous phase and therefore such stresses relieved.

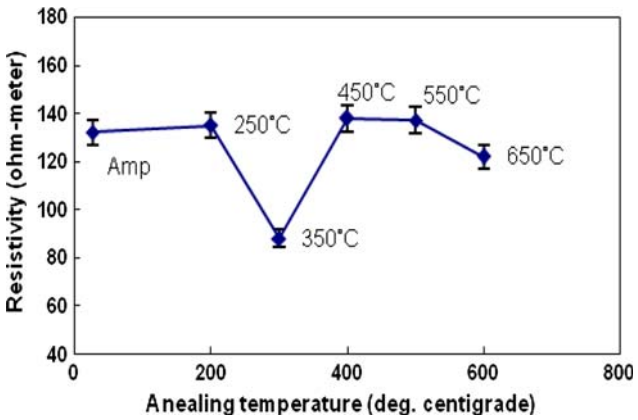

Fig. 3 Resistivity measurements of the amorphous samples and the annealed samples at various temperatures

Figure 4 shows the impedance data, plotted, and analyzed as Nyquist plots. The results showed that all of the plots consist of two capacitive loops, indicating the presence of activities of both electron-transfer and film-diffusion processes. The results of the EIS measurements indicated that the corrosion process was governed not only by electrochemical reaction steps, but also by diffusion steps (Fig. 4).

Several circuit arrangements were tested in order to evaluate the experimental results. The best fitting was obtained using the equivalent circuit shown in Fig. 5. This circuit is composed of three capacitive loops. The loop at the highest frequency range represents the double layer capacity and the charge transfer resistance. The second capacitive loop involves the oxide layer formed on the alloy surface. Finally, the loop at the lowest frequency range is very difficult to analyze because it cannot be seen completely. In this

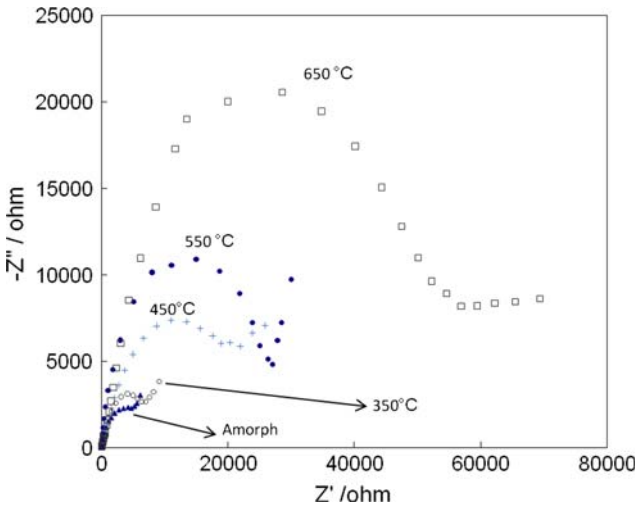

Fig. 4 Nyquist plots for the finemet alloy remained for 1 h in 0.10 M NaOH solution at 25 °C

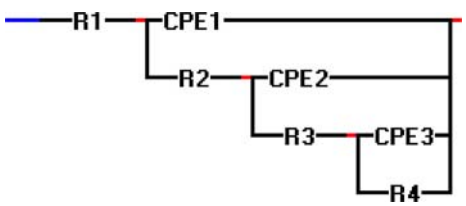

Fig. 5 Equivalent circuit for the finemet alloy

equivalent circuit, the constant phase elements were used instead of capacitors. In real electrochemical cells, capacitors show a phase angle of less than 90°. Several theories have been proposed to explain the reason for the non-ideal behavior of the double layer like microscopic surface roughness [18], presence of a porous corrosion product layer [19], or non-uniform distribution of current density on the surface [8, 23], but it has not been accepted universally. In such cases, the impedance of CPE has the form:

$$Z = Q(Jw)^{-\alpha} \quad (2)$$

where, Z is the impedance of electrode, w is the frequency at which the imaginary impedance reaches a maximum for the respective time constant, and Q is the pseudo capacitance of the system.

The charge transfer resistance of a material is related to its electrochemical activity. Comparison of the obtained results for different temperatures (Fig. 4) showed that the resistance increases with the increase in temperature. It is important to notice that nanocrystallized finemet alloy reveals the highest charge transfer resistance value compare to amorphous alloy; thereby, it is the most resistant alloys to corrosion.

Also, the EIS results showed that the charge transfer resistance varies with the annealing temperature (Fig. 4). Before relaxation at 350 °C, trivial changes in the charge transfer resistance of the alloy occurred. Annealing at higher temperatures caused a significant change in the charge transfer resistance due to structural relaxation. Further increasing in the annealing temperature caused more changes in the charge transfer resistance due to onset and completion of nanocrystallization. Also, the double layer capacitances of the alloy slightly increased before the beginning of nanostructure formation. After nanostructure formation, the double layer capacitance of the alloys significantly elevated due to interface increase. These results are in agreement with the XRD and resistivity results. Accordingly, it can be concluded that both relaxation and nanocrystallization improve corrosion behavior; however, nanocrystallization seems to be more effective than structural relaxation.

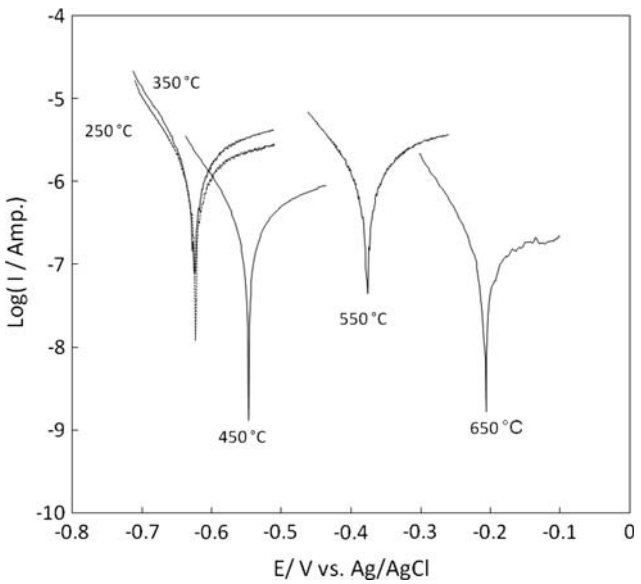

Fig. 6 Comparison of Tafel plots data recorded using linear sweep voltammetry at the scan rate of 1 mV s^{-1} after 1 h remaining in 0.10 M NaOH solution

Figure 6 presents Tafel plots of the alloy samples in 0.10 M NaOH solution. According to the values of the relevant parameters, including corrosion potential, corrosion current density, and polarization resistance, shown in Table 1, it can be concluded that the corrosion resistance of the samples increases as the annealing temperature increased. The obtained results also indicate that the increase in the annealing temperature shifts the corrosion potential anodically. The kinetic parameters such as corrosion potential, cathodic Tafel slope, and corrosion current density were calculated from Fig. 6. The obtained results are summarized in Table 1, and show Tafel slopes as 0.03 V dec^{-1} that are independent of temperature increase. A shift of the Tafel line toward the upper left of the diagram indicates an increase in both the resistance to corrosion and the corrosion current density of the samples.

Figure 7a, c illustrates the optical micrograph of the sample alloys annealed at 350 and 650 °C, respectively. It is clear that the samples annealed at 350 and 650 °C are both smooth and uniform, and rapid solidified cast morphology features can be observed. However, surface

Table 1 Data extracted from the Tafel plots (Fig. 6)

Temperature (°C)	I_{corr} (A cm^{-2})	B_c (V dec^{-1})	E_{corr} (V)	R_p (Ω)	Tafel coefficients
250	5.09E−07	0.029	−0.623	1.44E+03	−0.99
350	2. 96E−07	0.037	−0.624	1.502E+03	−0.99
450	6.04E−08	0.03	−0.547	5.042E+03	−0.99
550	3.339E−08	0.034	−0.372	2.09E+03	−0.95
650	1.37E−08	0.013	−0.206	6.544E+03	−0.99

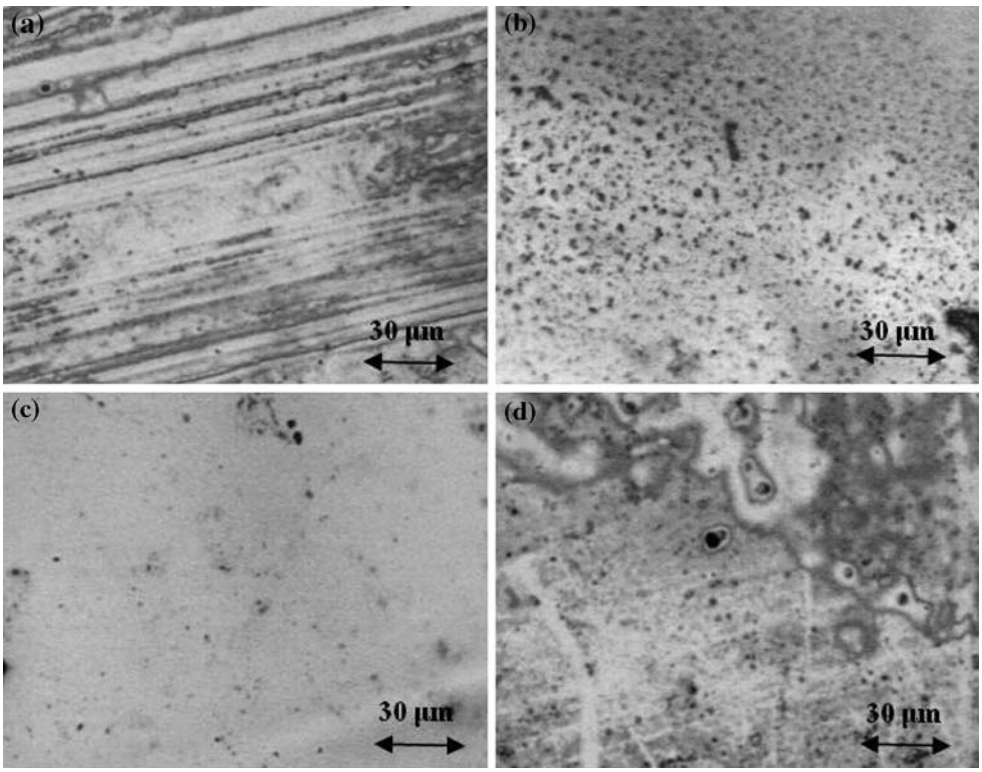

Fig. 7 Optical micrographs of the finemet alloy; **a** the annealed samples at 350 °C before corrosion, **b** after corrosion, **c** the annealed sample at 650 °C before, and **d** after corrosion

morphology of the sample annealed at 650 °C is smoother than the sample annealed at 350 °C. These may explain why the sample annealed at 650 °C shows the best anti-corrosion performance. Surface morphology of the samples after electrochemical corrosion is shown in Fig. 7b, d. It shows that corrosion features on the sample annealed at 350 °C are clearly more than on the sample annealed at 650 °C and also corrosion occurred regularly all over the surface of the former sample (Fig. 7b).

The enhanced resistance to oxidation in finemet alloy after annealing at higher temperatures could be explained according to its nanocrystalline structure [24, 25]. As mentioned above, this alloy contains a mixture of FeSi nanoparticles in its amorphous matrix, which has large number of interface boundaries that cause fast diffusion of the atoms especially at higher temperatures. Therefore, with increasing the temperature, the Si atoms in the FeSi nanograins segregate to interface boundaries where they can diffuse to the surface of the sample. At the surface, Si interacts with oxygen to form a passive layer of SiO_2, which hinders further oxidation [26].

Finally, nanocrystallization in amorphous finemet alloy not only improves its soft magnetic properties, but also appreciably improves its corrosion behavior, which is an important feature of this alloy for application.

Conclusion

Crystallization sequence of finemet alloy includes two different stages; in the first stage amorphous alloy converts into ultrafine FeSi grains embedded in the amorphous matrix. In the second stage, by increasing the annealing temperature, the residual amorphous matrix converts into Fe, Nb, and B compounds, which are destructive and must be avoided. In addition, the structural relaxation of as-quenched samples occurs at around 350 °C. Corrosion behavior of the alloy depends directly on its microstructure evolution. Annealing up to 350 °C has no effect on its structure and electrochemical response. Further increase in the annealing temperature noticeably improves corrosion behavior of the alloy due to both structural relaxation and nanocrystallization. However, it seems that nanocrystallization is more effective than structural relaxation.

References

1. Cheng JB, Liang XB, Xu BS, Wu YX (2009) J Mater Sci 44:3356. doi:10.1007/s10853-009-3436-5
2. Fujii H, Yardley VA, Matsuzaki T, Tsurekawa S (2008) J Mater Sci 43:3837. doi:10.1007/s10853-007-2220-7

3. Zhang YR, Ramanujan RV (2006) J Mater Sci 41:5292. doi: 10.1007/s10853-006-0263-9
4. Yoshizawa Y, Oguma S, Yamauchi K (1988) J Appl Phys 64:6044
5. McHenry ME, Willard MA, Laughlin DE (1999) Prog Mater Sci 44:291
6. Herzer G (1996) J Magn Magn Mater 157–158:133
7. Herzer G (1997) Handbook of magnetic materials, vol 10. Elsevier, Amsterdam, pp 417–461
8. Souza CAC, Politi FS, May JE, Kuri SE, Kiminami CS (1999) J Non-Cryst Solids 247:69
9. May JE, Souza CAC, Morelli CL, Mariano NA, Kuri SE (2005) J Alloys Compd 390:106
10. Mariano NA, Souza CAC, May JE, Kuri SE (2003) Mater Sci Eng 354:1–5
11. Petzold J (2002) J Magn Magn Mater 242–245:84
12. Hasegawa R (2006) J Magn Magn Mater 304:187
13. Altube A et al (2003) Corros Sci 45:685
14. Vara G et al (2007) J Non-Cryst Solids 353:1008
15. Marzo FF et al (2007) J Non-Cryst Solids 353:875
16. Marzo FF et al (2002) Electrochim Acta 47:2265
17. Altube A, Pierna AR (2004) Electrochim Acta 49:303
18. Rammelt U, Reinhard G (1988) Electrochim Acta 35–6:L199
19. Park JR, Macdonald DD (1983) Corros Sci 23:295
20. Garcia JA et al (2006) J Non-Cryst Solids 352:5118
21. Fiorillo F (2004) Measurement and characterization of magnetic materials. Elsevier, Amsterdam, pp 51–60
22. Kaevitser EV (2004) Mater Sci Eng A 375–377:683
23. Macdonald DD, Mckubre MCH (1982) Modern aspects of electrochemistry, vol 14. Plenum Press, New York, p 61
24. Miguel C, Kaloshkin S, Gonzalez J, Zhukov A (2003) J Non-Cryst Solids 329:63
25. Lovas A, Kiss LF, Balogh I (2000) J Magn Magn Mater 215–216:463
26. Poole CP (2003) Introduction to nanotechnology. Wiley, Hoboken, NJ, p 147